ON THE RELATIONSHIP BETWEEN LARGE-SCALE VORTICAL STRUCTURES AND SCALAR TRANSPORT PROCESSES IN A CONTROLLED CONFINED COAXIAL JET

Akihiko Mitsuishi, Koji Fukagata, and Nobuhide Kasagi
Department of Mechanical Engineering,
The University of Tokyo,
Hongo 7-3-1, Bunkyo-ku, Tokyo 113-8656, JAPAN
mituisi@thtlab.t.u-tokyo.ac.jp, fukagata@thtlab.t.u-tokyo.ac.jp, and kasagi@thtlab.t.u-tokyo.ac.jp

ABSTRACT

We carry out direct numerical simulation (DNS) of scalar transport and mixing in a coaxial jet issued into a small model combustor. Analysis is made on the detailed mechanism of mixing enhancement achieved by an active control of the near-field large-scale vortical structures. The main interest lies in the relationship between these vortical structures and associated scalar transport processes in the near field downstream of the nozzle exit. From the phase-averaged statistics, the mechanism of mixing enhancement is revealed in the case of the best mixing achieved.

INTRODUCTION

A coaxial jet flow is widely used in industrial applications, such as gas turbine combustors and other chemical reactors, where mixing of different fluids takes place. There are a number of options to passively control the flow field inside such equipment (*e.g.,* swirlers and non-circular nozzles) to improve its performance at the design point. However, if we aim at small-scale power generation, *i.e.,* distributed generation systems, the power output often shifts off the design point. In such cases, passive control methods are no longer effective and we need to rely on some active control methods.

Previous experimental studies have demonstrated that the performance of a coaxial jet combustor can be controlled by active manipulation of the near-field large-scale vortical structures and transport of reactants. Suzuki *et al.* (2004) developed a special nozzle called "intelligent nozzle," which can manipulate the near-field vortical structures in the jet. It has distributed electromagnetic flap actuators mounted on the periphery of the outer nozzle, as shown in Fig. 1. With this
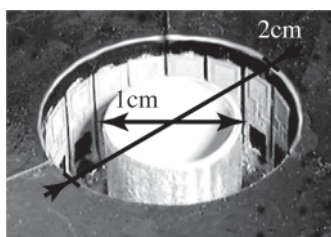

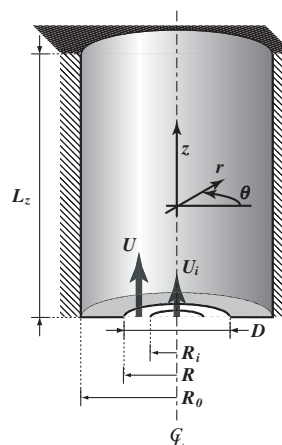Figure 1: Intelligent nozzle (Suzuki *et al.*, 2004).

Figure 2: Computational model.

Table 1: Basic conditions.

R/R_i	R_0/R	U/U_i
2	2	6.396

nozzle, Kurimoto (2005) successfully stabilized the flame inside a small model combustor. He also experimentally examined the effect of different motions of the actuators on the flow field. However, basic transport mechanism in the controlled coaxial jet flow should be clarified in detail to achieve more flexible control with this nozzle.

The objective of the present study is to investigate the scalar transport mechanism controlled by the axisymmetric mode of the intelligent nozzle (Kurimoto, 2005). In order to analyze this controlled jet flow, we carry out direct numerical simulation (DNS). First, we investigate the effect of control parameters on the flow and scalar fields. Then, we discuss the near-field transport processes of momentum and scalar in the case of the best mixing.

NUMERICAL METHOD

Figure 2 shows the computational model used in this study. The flow domain is confined by lateral and bottom walls. The geometric and flow conditions are listed in Table 1. The
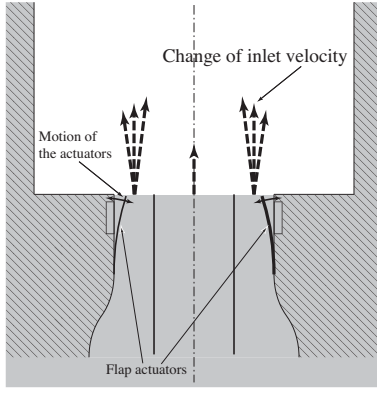
Figure 3: Motion of actuators and change of inlet velocity profile.

governing equations are the incompressible continuity and Navier-Stokes equations and the transport equation of a passive scalar:

$$\nabla \cdot \mathbf{u} = 0 \tag{1}$$

$$\frac{\partial \mathbf{u}}{\partial t} = -\nabla \cdot (\mathbf{u}\mathbf{u}) - \nabla p + \frac{1}{\mathrm{Re}} \nabla^2 \mathbf{u} \tag{2}$$

$$\frac{\partial c}{\partial t} = -\nabla \cdot (c\mathbf{u}) + \frac{1}{\mathrm{Re} \cdot \mathrm{Sc}} \nabla^2 c \tag{3}$$

Here, $\mathbf{u}$, p, and c denote dimensionless velocity vector, pressure, and passive scalar concentration, respectively. All variables related to the flow are normalized by the bulk mean velocity of the annular jet, U, and the outer nozzle diameter, D. The mixing fraction of the central jet fluid is represented by c. Focusing on a small CH_4-Air combustor, of which power output is 0.5-1 kW, the Reynolds number, Re, based on U and D is set at 1320. The Schmidt number, Sc, of the passive scalar is assumed to be unity, which nearly corresponds to the diffusion of CH_4 into air under the standard temperature and pressure. The governing equations are numerically solved by the finite difference method on the cylindrical coordinates (Fukagata and Kasagi, 2002) with (65, 64, 257) grid points in (r, θ, z) directions. In addition, we use the TVD scheme (Harten, 1984) for the advection term of the scalar transport equation.

We focus on the axisymmetric mode of the intelligent nozzle, *i.e.,* in-phase motion of all actuators. A schematic diagram of the control effect is shown in Fig. 3. In the present simulation, we model the motion of actuators as a change of an inlet velocity profile. The volumetric flow rate is kept constant and the outer nozzle radius is contracted sinusoidally as:

$$R_{ctrl}(t) = R - \varepsilon\left(1 - \cos\left(2\pi \, \mathrm{St}_{ctrl} t\right)\right) \tag{4}$$

The dimensionless control frequency and amplitude are St_{ctrl} and ε, respectively, and the axial (u_z) and radial (u_r) velocity at the jet exit are given as follows:

$$u_z(r,\theta,0,t) = U_0\left(r; R_{ctrl}(t), R_i\right) \Big/ \frac{R_{ctrl}(t)^2 - R_i^2}{R^2 - R_i^2} \tag{5}$$

$$u_r(r,\theta,0,t) = \frac{dR_{ctrl}(t)}{dt} = -2\pi \, \mathrm{St}_{ctrl} \varepsilon \sin\left(2\pi \, \mathrm{St}_{ctrl} \, t\right) \tag{6}$$

Here, the analytical solution of laminar velocity profile in an annular pipe, of which outer and inner radii are a and b, is denoted as $U_0(r;a,b)$. The profile of $U_0(r;a,b)$ is derived from the Navier-Stokes equation as follows:

$$U_0(r;a,b) \equiv -\frac{\mathrm{Re}}{4}\frac{dp}{dz}\left\{a^2 - r^2 - \frac{\ln a/r}{\ln a/b}\left(a^2 - b^2\right)\right\} \tag{7}$$

The inlet velocity profile of the inner jet is kept parabolic during the control.

For the definition of the phase-average operation, we employ the following decomposition to an instantaneous value, $\tilde{g}$, of any quantity, g:

$$\tilde{g} = \langle g \rangle_\phi + g' \tag{8}$$

where $\langle g \rangle_\phi$ is the phase-average, which is the summation of the time mean and the periodic component at the phase of ϕ, *i.e.,*

$$\langle g \rangle_\phi \equiv \lim_{N \to \infty} \frac{1}{N} \sum_{n=1}^{N} \left[\tilde{g}\left(\phi + 2n\pi \, \mathrm{St}_{ctrl} t\right)\right] \tag{9}$$

and g' is the other random component. The phase-averaged r.m.s. fluctuations of $\tilde{g}$ is then defined as:

$$\langle g \rangle_{\phi,rms} \equiv \left\langle g'^2 \right\rangle_\phi = \lim_{N \to \infty} \frac{1}{N} \sum_{n=1}^{N} \left[g'^2\left(\phi + 2n\pi \, \mathrm{St}_{ctrl} t\right)\right] \tag{10}$$

All the phase-averaged statistics are finally averaged in the θ direction.

EFFECTS OF CONTROL PARAMETERS

In Fig. 4, instantaneous vortical structures and concentration of the scalar ejected from the central nozzle are visualized in the natural and controlled jets in order to grasp rough features of the above control method. The control amplitude and frequency are $\varepsilon = 0.0125$ and $\mathrm{St}_{ctrl} = 1$, at which the best mixing is observed in the experiments by Kurimoto *et al.* (2001). The vortical structures are identified by the second invariant of the deformation rate
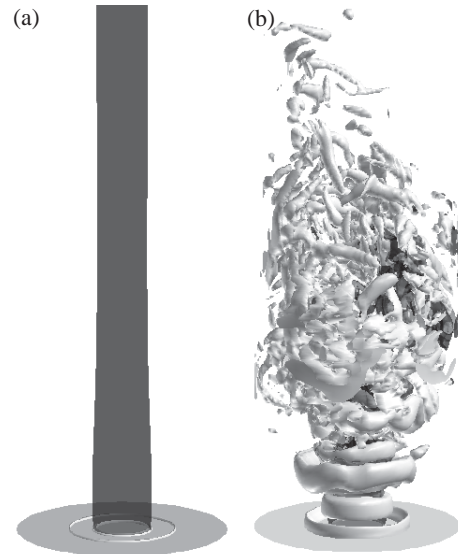

Figure 4: Instantaneous vortical structures (white) and scalar concentration distributions (black).
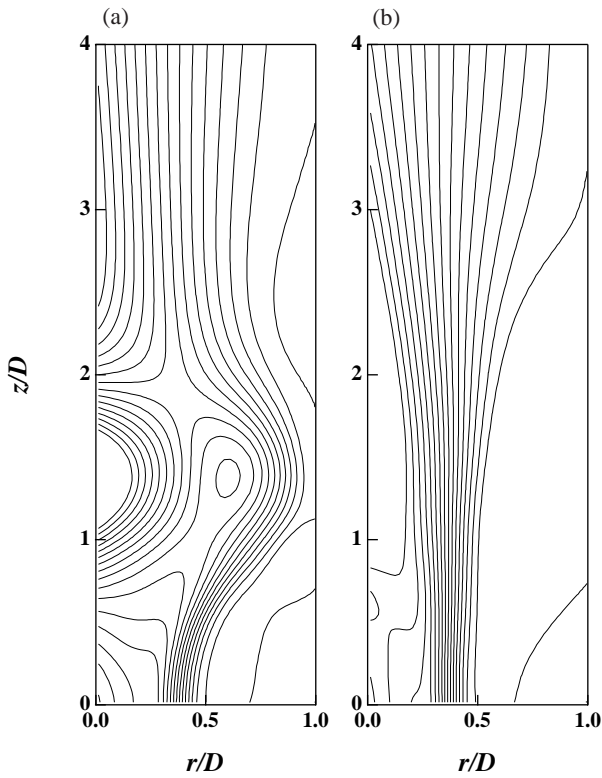(a) natural jet; (b) controlled jet ($\mathrm{St}_{ctrl} = 1$, $\varepsilon = 0.0125$).

Figure 5: Streamlines of mean velocity field for different control amplitudes: (a) $\varepsilon = 0.001$ and (b) $\varepsilon = 0.01$.
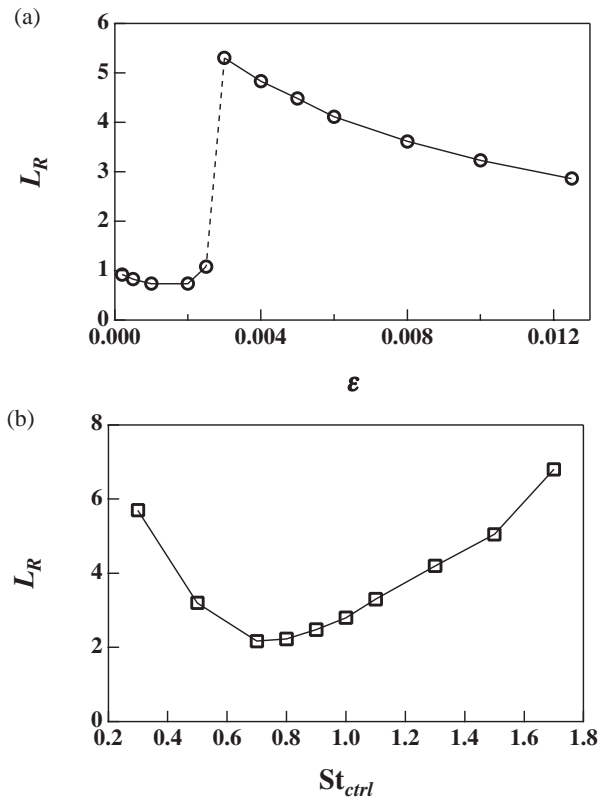

Figure 6: The relations between the reattachment length and each control parameter: (a) control amplitude and (b) control frequency.

tensor. Without control, mixing between the the central jet and the ambient fluid is very poor. A similar flow pattern is also observed in a confined annular jet of low Reynolds numbers in previous experimental work (Sheen *et al.*, 1997). With control, large-scale vortex rings are generated in the near field of the nozzle and they promptly break down intensifying the scalar mixing.

In order to understand the characteristics of the present control method, we first investigate the effects of ε and St_{ctrl} on the flow field. Figure 5 shows streamlines of the mean velocity fields in the r-z plane with relatively small ($\varepsilon = 0.001$) and large ($\varepsilon = 0.01$) control amplitudes. The control frequency is kept constant at $St_{ctrl} = 1$. Note that the left and right edges of each graph correspond to the central axis and lateral wall, respectively. The radial positions of $r/D = 0.25$ and 0.5 are the inner and outer shear layers of the intelligent nozzle, respectively. The streamlines are dispersed uniformly at $z/D = 6$ in both cases. This means that, despite the large difference in ε, the momentum is well exchanged between the central and annular jets within the computational domain. However, the upstream flow structures are considerably different. In the case with smaller ε, the annular flow reattaches to the lateral wall in a shorter distance from the nozzle. The annular flow detaches soon after this reattachment point and forms a recirculation zone on the central axis. From these observations, the reattachment length of the annular jet is considered as a quantity that characterizes the flow structure.

Figure 6 shows the relation between the reattachment length, L_R, and each control parameter. The reattachment length is defined as a streamwise distance between the nozzle exit and the reattachment point on the lateral wall. Figure 6 (a) shows the relation between L_R and ε. The reattachment length is much shorter in the cases of $\varepsilon \leq 0.0025$ than $0.003 \leq \varepsilon$ as already shown in Fig. 5., and there is a sudden jump in L_R as ε changes from 0.0025 to 0.003. This indicates that the flow structure changes discontinuously as ε changes. If ε is greater than 0.003, L_R decreases monotonically as ε increases. Moreover, the effect of ε becomes smaller and smaller. For further discussions, ε is fixed at 0.0125 referring to the previous experiment (Kurimoto, 2001). Similarly, the relation between L_R and St_{ctrl} is shown Fig. 6 (b). However, the reattachment length depends strongly on the St_{ctrl} in every case studied.

Figures 7 (a)-(c) show the mean scalar distributions in the r-z plane under the control with three different frequencies, *i.e.*, St_{ctrl} is 0.3, 1, and 1.7. Note that, in these figures, the right edge of each graph corresponds to the position of $r/D = 0.5$, namely
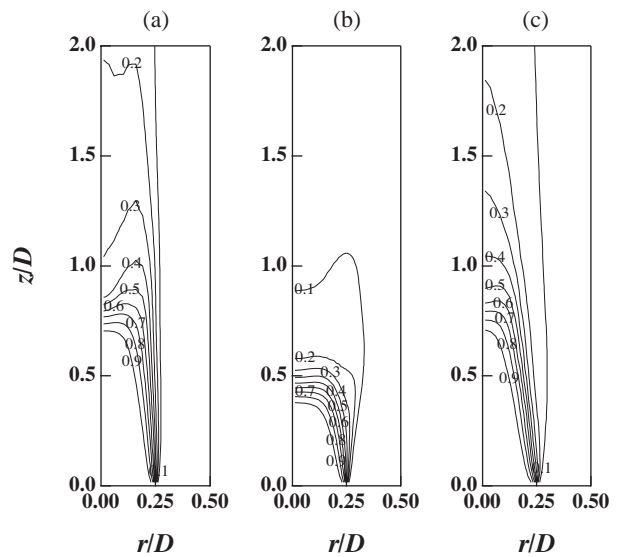

Figure 7: Mean scalar distribution at the different control frequency: (a) $St_{ctrl} = 0.3$, (b) $St_{ctrl} = 1$, and (c) $St_{ctrl} = 1.7$.
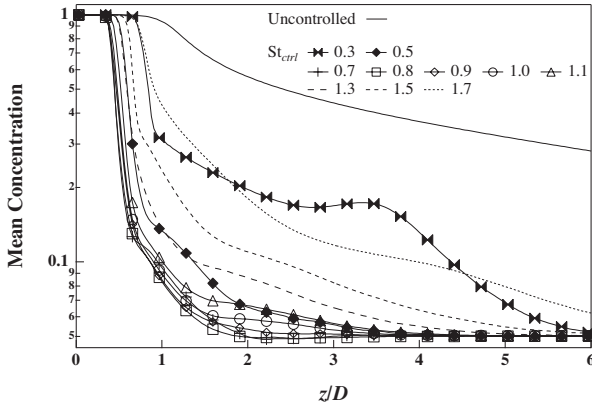
Figure 8: Effect of control frequency on the mean scalar concentration along the central axis.

the outer shear layer of the nozzle. The scalar is mostly transported in the axial direction. This fact makes the survey of St_{ctrl} much easier. The axial mean concentration profile along the central axis can represent the characteristics of the scalar field.

The effects of control frequency on the mean scalar concentration along the central axis are shown in Fig. 8. Regardless of the frequency selected, better mixing is obtained than uncontrolled case. Figures 6, 7, and 8 suggest that the cases studied are classified into three regimes:

(i) $St_{ctrl} < 0.7$
(ii) $0.7 \leq St_{ctrl} \leq 1.1$
(iii) $1.1 < St_{ctrl}$

The regime of (ii) achieves the best mixing along the central axis among all tested St_{ctrl}. This tendency is relatively independent of St_{ctrl} compared to the group of (i) and (iii). This means that, for these cases, the mixing enhancement is achieved by a certain mechanism which is not affected by St_{ctrl}. For the following analysis of the mixing enhancement in the controlled flow field, we choose $St_{ctrl} = 0.9$ as a representative of this group.

The other regimes are explained briefly. Regime (i) is characterized by a restoration of the concentration downstream from the dilution around $z/D < 1$. The case of $St_{ctrl} = 0.3$ gives an especially clear hump at $z/D = 3.5$. In (iii), the mixing along the

central axis is suppressed. Unlike (i), the central concentration decreases monotonically without any humps.

SCALAR TRANSPORT AND VORTEX DYNAMICS

Here we focus on the control mechanism of the scalar transport for the case of $\varepsilon = 0.0125$ and $St_{ctrl} = 0.9$, where the strongest enhancement of mixing along the central axis was achieved. The phase-averaged statistics of vortical motions and scalar concentration are examined to analyze this mechanism.

The distribution of the phase-averaged azimuthal vorticity, $\langle \omega_\theta \rangle_\phi$, in the r-z plane is shown in Fig. 9 for five differentint control phases, i.e., ϕ is 0, 0.4π, 0.8π, 1.2π, and 1.6π. It indicates how the present control method generates the large-scale vortical structures in the near-field. They are basically two-dimensional ring-like structures. We can clearly see that a pair of counter-rotating vortex rings are discharged at the same rate as the control frequency. This roll-up of the inner and outer shear layers is primary effect of the present control.

The inner roll-up vortex ring reels the central jet fluid and carries plenty of scalar. Figure 10 depicts $\langle \omega_\theta \rangle_\phi$ together with $\langle c \rangle_\phi$ in the r-z plane at the same phases as Fig. 8. The scalar is captured by the inner vortex ring, not the outer, and convected downstream. From these observations, the scalar mixing mechanism along the central axis observed in Fig. 8 can be explained. First, scalar is ejected from the central nozzle. The scalar cannot go further downstream along the central axis, because the central flow is stagnated by the reversing flow induced by the inner vortex ring. The scalar is then wound up by the inner vortex ring.

Distributions of the phase-averaged r.m.s. fluctuations of the radial and axial vorticity are shown in Fig. 11 for one representative phase, i.e., $\phi = 1.6\pi$, in order to study the spatial development of the azimuthal vortical structures in the downstream region. These values indicate how the initially two-dimensional large-scale vortex rings break up and transform into three-dimensional structures. A remarkable observation is that ω_z is highly localized, e.g., at $(r/D, z/D) \cong (0.1, 0.8)$ and $(0.6, 1.3)$, while ω_r is not. This means that the streamwise vortical structures arise from specific places, while ω_r results from relatively random motion of the broken vortices downstream. Namely, the streamwise vortical structures generated by some specific mechanisms are important in spatial development of the vortex rings. In fact, some mechanisms of emergence of the
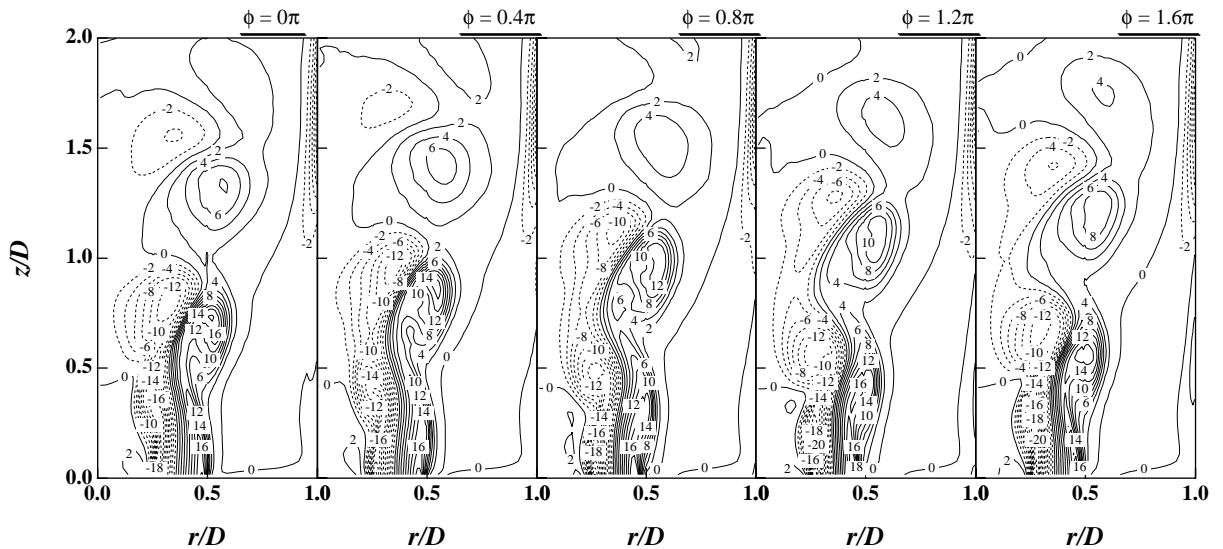

Figure 9: Near-field vortical structures generated by the control of $\varepsilon = 0.0125$ and $St_{ctrl} = 0.9$: phase-averaged azimuthal vorticity with solid (broken) lines for positive (negative) value.
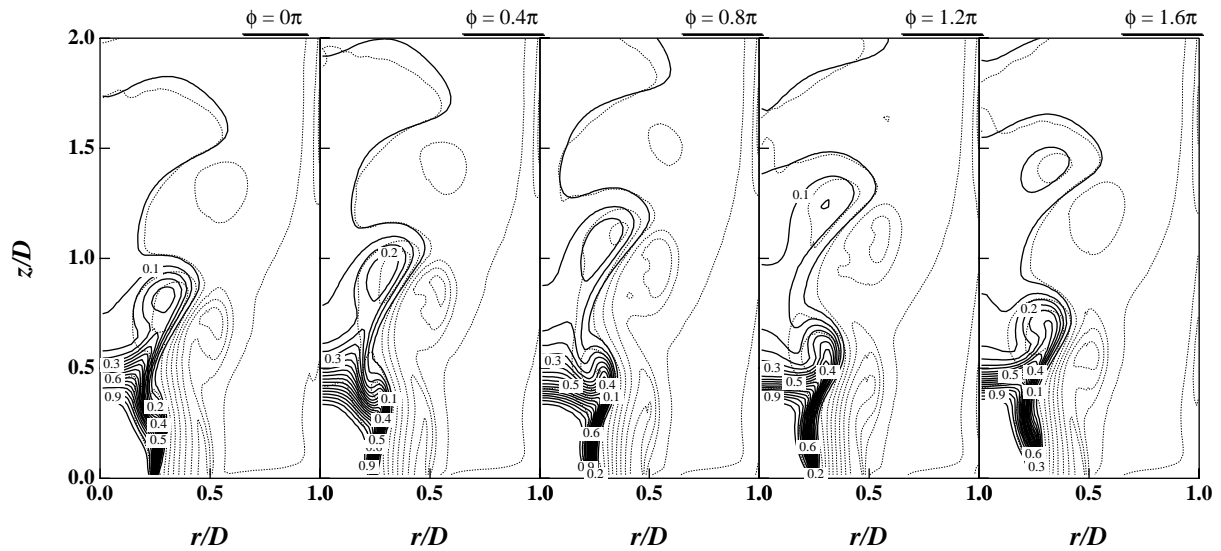
Figure 10: Scalar concentration transported by near-field vortex rings: Phase-averaged scalar concentration (bold solid lines) and azimuthal vorticity (dotted lines). $\varepsilon = 0.0125$; $St_{ctrl} = 0.9$.
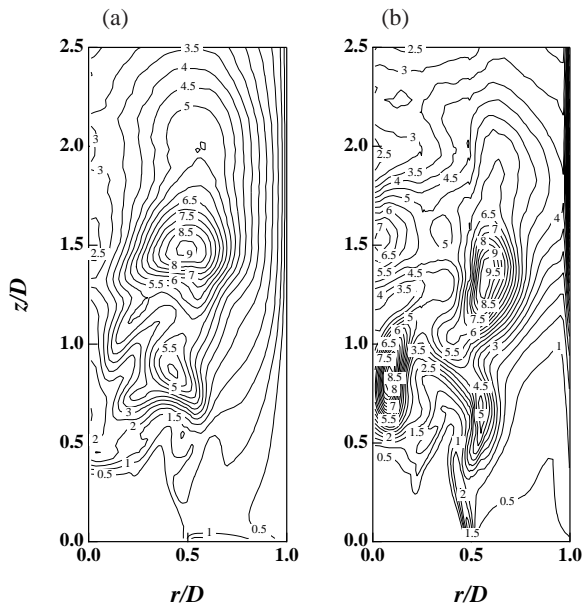

Figure 11: Phase-average r.m.s. value of (a) radial and (b) streamwise vorticity. $\varepsilon = 0.0125$; $St_{ctrl} = 0.9$; $\phi = 1.6\pi$

streamwize vortical structures in a free shear layer has been discussed by many researchers (see, *e.g.,* Pierrehumbert and Widnall, 1982 and Lin and Corcos, 1984). These structures are called 'rib vortices.' The rib vortices arise from high shear regions between spanwise vortical structures such as the vortex rings that are depicted in Fig. 9.

To confirm whether the peaks in Fig. 11 correspond to the rib vortices, the components of $\langle \omega_\theta \rangle_\phi$ and $\langle \omega_z \rangle_{\phi,rms}$ are shown together in Fig. 12. One of the peaks of $\langle \omega_z \rangle_{\phi,rms}$ ((A) in Fig. 12) exists between the inner vortex rings and stretched due to the induced velocity of the inner vortex rings. This fact means that the peak of $\langle \omega_z \rangle_{\phi,rms}$ originates from the rib vortices. On the other hand, another peak of $\langle \omega_z \rangle_{\phi,rms}$ ((B) in Fig. 12) is in the region of the outer vortex ring. A close-up picture near this region is given in Fig. 13. It clearly shows that the corresponding three-dimensional structures (A) are streamwise vortices, while those of (B) are a consequence of the distortion of the outer vortex rings. Thus, the rib vortices play an important role to change the inner vortex rings from two- to three-dimensional shapes and consequent break down of the vortex rings. Therefore, the three-dimensionalization of scalar transported by the inner vortex ring is closely related to the emergence of the rib vortices. Although
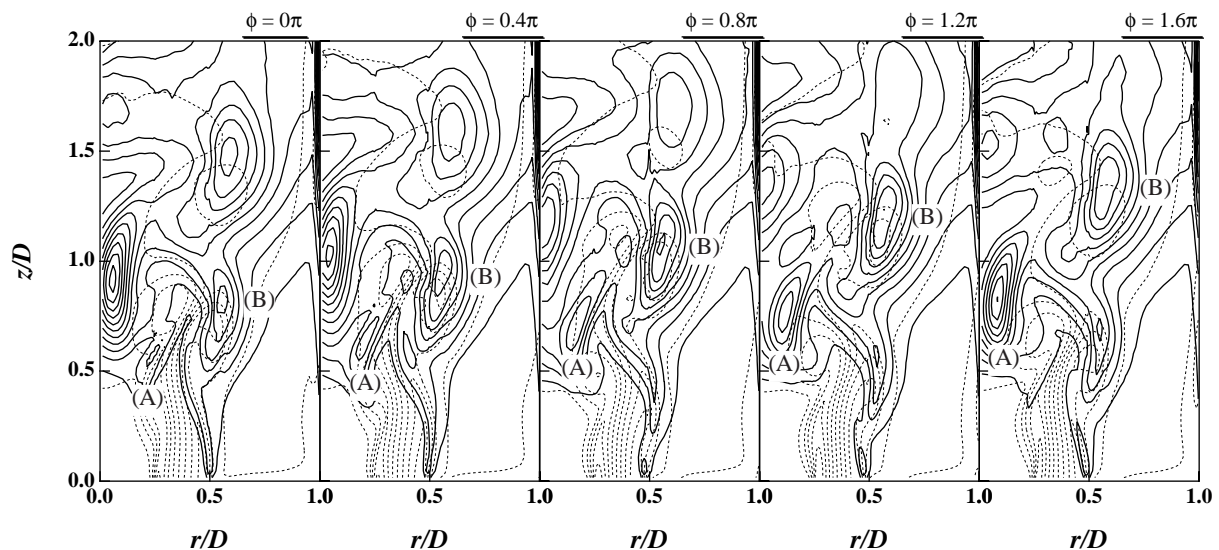

Figure 12: Phase change of the streamwise vortical structures and the vortex rings: Phase-averaged rms fluctuations of axial vorticity (bold solid lines) and azimuthal vorticity (dashed lines). $\varepsilon = 0.0125$; $St_{ctrl} = 0.9$.

not shown here, results we obtained from the spectral analysis in the θ direction also support that the emergence of the rib vortices is closely related to the three-dimensionalization of the inner vortex rings.

CONCLUSIONS

DNS of controlled confined coaxial jet flow has been carried out. The following conclusions are derived on the control of near-field vortical structures and the consequent scalar transport processes.

The effects of the control method of periodic contraction of the nozzle radius are surveyed. Flow manipulation with this control can generate various type of flow patterns and concentration profiles depending on the amplitude and the frequency of the contraction.

The mechanism of mixing enhancement with the intelligent nozzle can be explained as follows. First, a pair of counter-rotating two-dimensional vortex rings are discharged synchronized with the control input. Next, the scalar ejected from the central nozzle is entrained by the inner vortex rings rolled up from the inner shear layer. The inner vortex rings that contain plenty of scalar are then distorted with the emergence of the rib vortices between the inner vortex rings. Finally, the initially two-dimensional inner vortex rings are transformed into three-dimensional structures, and they break down to enhance the mixing of scalar concentration.

References

Fukagata, K. and Kasagi, N., 2002, "Highly Energy-Conservative Finite Difference Method for the Cylindrical Coordinate System," *Journal of Computational Physics*, Vol. 181, pp. 478-498.

Harten, A., 1984, "On a Class of High Resolution Total-Variation-Stable Finite Difference Schemes," *SIAM Journal on Numerical Analysis*, Vol. 21, pp. 1-23

Kurimoto, N., 2005, Ph.D. Thesis, The University of Tokyo, Tokyo.

Kurimoto, N., Suzuki, Y., and Kasagi, N., 2001, "Control of Coaxial Jet Mixing and Combustion with Arrayed Micro Actuators," *Proc. 5th World Conf. Exp. Heat Trans., Fluid Mech., and Thermodyn.*, pp. 511-516.

Lin, S. J. and Corcos, G. M., 1984, "The Mixing Layer: Deterministic Models of a Turbulent Flow. Part 3. The Effect of Plane Strain on the Dynamics of Streamwise Vortices," *Journal of Fluid Mechanics*, Vol. 141, pp. 139-178.

Pierrehumbert, R. T. and Widnall, S. E., 1982, "The Two- and Three-Dimensional Instabilities of a Spatially Periodic Shear Layer," *Journal of Fluid Mechanics*, Vol. 114, pp. 59-82.

Sheen, H. J., Chen, W. J., and Wu, J. S., 1997, "Flow Patterns for an Annular Flow Over an Axisymmetric Sudden Expansion," *Journal of Fluid Mechanics*, Vol. 350, pp. 177-188.

Suzuki, H., Kasagi, N., and Suzuki, Y., 2004, "Active Control of an Axisymmetric Jet with Distributed Electromagnetic Flap Actuators," *Experiments in Fluids*, Vol. 36, pp. 498-509.

Figure 13: Instantaneous vortical structures (white opaque) and scalar isosurface (gray transparent).